Icarus 386 (2022) 115166

Contents lists available at ScienceDirect

Icarus

journal homepage: www.elsevier.com/locate/icarus

Formation age of lunar Lalande crater and its implications for the source region of the KREEP-rich meteorite Sayh al Uhaymir 169

Luyuan Xu [a,b], Le Qiao [c,*], Minggang Xie [d], Yunhua Wu [e]

[a] State Key Laboratory of Lunar and Planetary Sciences, Macau University of Science and Technology, Macau, China
[b] CNSA Macau Center for Space Exploration and Science, Macau, China
[c] Shandong Key Laboratory of Optical Astronomy and Solar-Terrestrial Environment, School of Space Science and Physics, Institute of Space Sciences, Shandong University, Weihai, Shandong 264209, China
[d] College of Science, Guilin University of Technology, Guilin 541006, China
[e] Planetary Environmental and Astrobiological Research Laboratory, School of Atmospheric Sciences, Sun Yat-sen University, Zhuhai 519082, China

ARTICLE INFO

Keywords:
Lalande crater
Formation age
Lunar meteorite
KREEP
Lunar/moon

ABSTRACT

As the most KREEP-rich lunar sample, the Sayh al Uhaymir (SaU) 169 meteorite would provide more valuable information concerning the KREEP and early lunar evolution of the Moon if its source regions can be pinpointed. Previous studies proposed Lalande crater as the source region that corresponds to the impact event of ~2.8 Ga recorded in SaU 169, whereas this linkage is highly dependent on the age determination of the potential source crater. By counting craters superposed on the ejecta blankets of Lalande and modelling the burial process of these superposed craters by Lalande's ejecta, we find that the crater statistics around Lalande are heavily influenced by the existing of pre-Lalande craters larger than ~170 m in diameter, which could lead to a largely overestimated age of Lalande crater. After taking this influence into consideration, we obtain that Lalande crater is a Copernican crater with a formation age of 410 ± 20 Ma, and the adjacent mare basalts unit has an Imbrian age of $3.8^{+0.04}_{-0.06}$ Ga. The formation age of Lalande crater is inconsistent with any of the radio-isotopic ages recorded in SaU 169, indicating that Lalande crater is unlikely to be the source region of this lunar meteorite.

1. Introduction

1.1. KREEP: The final product of lunar magma ocean crystallization

The prevalent model for the early evolution of the Moon envisions a global surface layer of molten silicates (lunar magma ocean) several hundred kilometers in depth (e.g., Wood et al., 1970; Smith et al., 1970). Sequential cooling and crystallization produce a range of cumulate lithologies with variable compositions, including dense mafic assemblages which sink to the magma ocean to form the lunar mantle and less-dense anorthosite cumulates which floated to the uppermost region to form the anorthositic lunar crust (e.g., Warren, 1985). The last residual (<~1%) melt became increasingly enriched in incompatible elements, especially potassium (K), rare earth elements (REE), and phosphorus (P), which crystallized to form the KREEP-rich cumulates sandwiched between the anorthositic crust and mafic mantle (Warren and Wasson, 1979; Shearer et al., 2006). As the final products of the lunar magma ocean crystallized, these KREEP-rich materials preserved critically important information concerning the evolution of the nascent Moon.

KREEP-rich rocks, though with a wide range of lithologies and compositions, have been identified in the sample collections of every single Apollo sample return mission (e.g., Heiken et al., 1991). Many scientists in the Apollo era anticipated that the KREEP layer is global in extent (e.g., Meyer Jr, 1977; Warren and Wasson, 1979). However, global orbital compositional mapping of the Moon in the 1990s quickly revealed that Apollo/Luna sampling sites can only represent a very small portion of lunar surface (e.g., Elphic et al., 1998). As thorium (Th) is typically abundant in KREEP-rich materials (Heiken et al., 1991), the spatial mapping of Th contents commonly serves as an adequate tracer for the distribution of KREEP in remote sensing studies (e.g., Lawrence et al., 1999). Global Th mapping efforts by the gamma-ray spectrometer onboard the Lunar Prospector mission unambiguously show that KREEP-rich materials are mainly concentrated in the western portion of the lunar nearside, a region termed Procellarum KREEP Terrane (PKT; Jolliff et al., 2000) and all Apollo/Luna missions landed in or near this anomalous PKT province. In addition, dozens of small areas of Th/

* Corresponding author.
E-mail address: leqiao.geo@gmail.com (L. Qiao).

https://doi.org/10.1016/j.icarus.2022.115166
Received 30 March 2022; Received in revised form 25 June 2022; Accepted 29 June 2022
Available online 2 July 2022
0019-1035/© 2022 Elsevier Inc. All rights reserved.

KREEP enhancements have been recognized across the lunar surface, including both farside and high-altitude regions (Lawrence et al., 2003). Therefore, our knowledge of KREEP derived from all returned samples are incomplete and somewhat biased. Additional lunar samples are needed for an improved understanding of the early evolution of the Moon.

1.2. Sayh al Uhaymir (SaU) 169 meteorite: The most KREEP-rich lunar sample

Lunar meteorites, rocks ejected from the Moon and subsequently fell on Earth surface, are another type of lunar samples that can be precisely analyzed in Earth laboratories. These meteorites are valuable supplementary to the existing returned Apollo/Luna samples and have uniquely advanced our understanding of the origin and evolution of the Moon (e.g., Korotev, 2005). Among the over 500 documented lunar meteorites (as of March 2022, based on the Meteoritical Bulletin Database: https://www.lpi.usra.edu/meteor/metbull.php), the Sayh al Uhaymir (SaU) 169 meteorite, found in the Al Wusta Governorate of Oman in 2002, has the most KREEP-enriched lithology (Russell et al., 2003). With a measured Th content of ~30 ppm (μg/g; Gnos et al., 2004; Korotev et al., 2009), the impact-melt breccias (IMBs) of SaU 169 are more KREEP-rich than the bulk chemistry composition of all Apollo and Chang'e-5 samples collected in the PKT terrain (e.g., Korotev, 2004; Tian et al., 2021; Li et al., 2022). Detailed laboratory high-precision and -accuracy measurements (chemical, mineralogical, petrologic, isotopic, and geochronologic) of this unique rock has revealed abundant information concerning the nature and evolution of lunar KREEP (e.g., Al-Kathiri et al., 2007; Lin et al., 2012; Liu et al., 2012; Tartèse et al., 2014; Xing et al., 2020; Zhang et al., 2019).

Nevertheless, the lack of precise geographical locations and geological context for the SaU 169 meteorite (as for almost all lunar meteorites) has seriously hindered the full interpretation of these detailed laboratorial measurements. Pinpointing the source region of this unique lunar piece on the Moon would be invaluable in advancing our understanding of the KREEP and early lunar evolution of the Moon.

Radio-isotopic dating analyses of the meteorite SaU 169 revealed a complicated sequence of four impact events with ages of ~3.9 Ga, ~2.8 Ga, ~200 Ma, and < 0.34 Ma (Gnos et al., 2004). Among these recorded ages, the ~3.9 Ga age is recognized to come from the Imbrium impact event, and the other ages are interpreted to represent subsequent impacts that disturbed the isotopic systematics of the sample.

Based on the compositional similarities between the KREEP-rich nature of the meteorite and the Procellarum KREEP Terrane, the source regions for the three younger ages recorded in this meteorite have been associated with the KREEP Terrane on the Moon. Gnos et al. (2004) initiated this source tracking effort and linked SaU 169 meteorite to Lalande crater, a 23-km-diameter crater located in the equatorial region of lunar nearside (4.46°S, 8.65°W), on the highlands southeast of Mare Insularum and northeast of Mare Necteria. The linkage between SaU 169 and Lalande crater is based on the analyses from three main aspects: 1) Lalande crater is located in one of the Th hot spots within the PKT region (Fig. 1a); 2) the Fe and Ti contents around Lalande are compatible with the bulk composition of the regolith of SaU 169; and 3) the absolute model age (AMA) of Lalande crater is highly consistent with the radio-isotopic Ar—Ar age of 2.8 Ga recorded in the meteorite. Obviously, this linkage is highly dependent on the age determination of Lalande crater, though the formation age of Lalande crater is still under debate. Baldwin (1985) conducted crater counts on the areas interior and on the rims of Lalande crater based on Lunar Orbiter images and obtained a model absolute age of 2.2–2.8 Ga (corresponding to the Eratosthenian Period within ~3.20- ~ 1.0 Ga; Stöffler and Ryder, 2001; Wilhelms et al., 1987), which is the age accepted by Gnos et al. (2004) for pinpointing source region of meteorite SaU 169. However, both the pronounced ray system and the well-preserved sharp rim crest of Lalande crater (Fig. 1b) support that it is highly likely to be a Copernican crater (<~1.0 Ga; Wilhelms et al., 1987; Stöffler and Ryder, 2001) rather than of Eratosthenian-era, although some ray craters can be older than ~1.0 Ga if their rays contain compositional distinct feldspar-rich ejecta (e.g., Hawke et al., 2004). In addition, the most recent lunar geologic map of Fortezzo et al. (2020), a unified global lunar geologic map at a 1:5,000,000-scale, also designated Lalande as a Copernican crater.

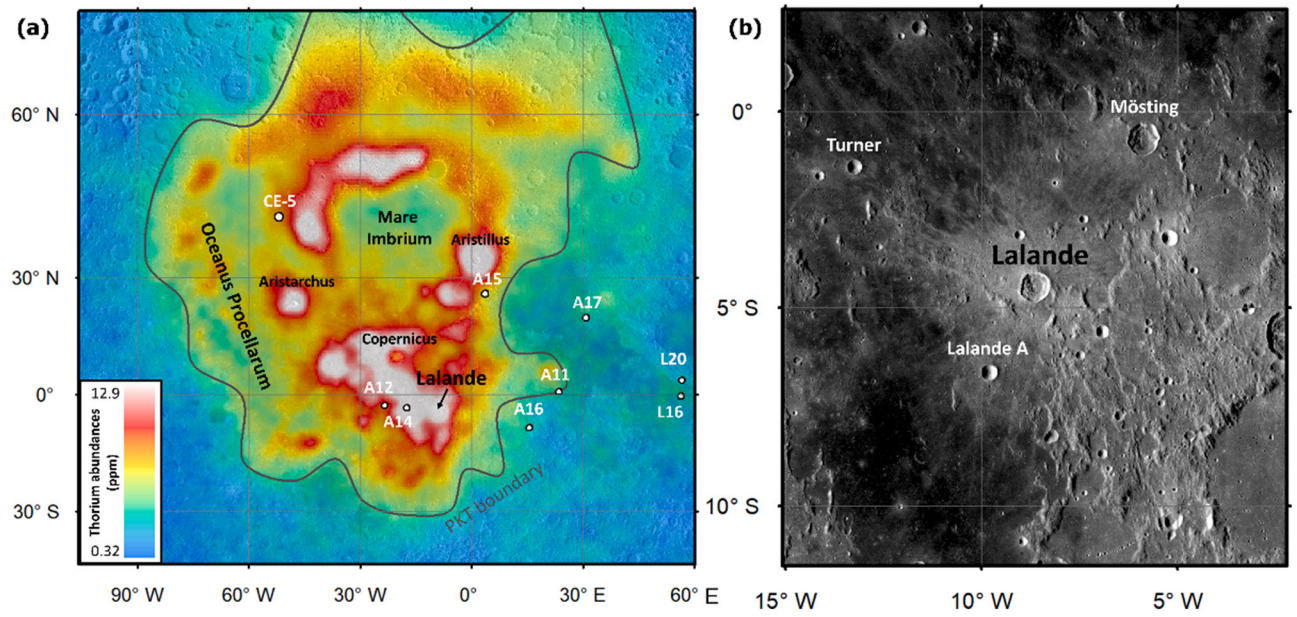


Fig. 1. Geologic context around Lalande crater. (a) Thorium (Th) composition distributions of Procellarum KREEP Terrane (PKT) with its boundary (Th = 3.5 ppm) outlined by the solid black curve. Lalande crater locates in one of the Th hot spots of this region. The base map is Lunar Reconnaissance Orbiter Wide-Angle camera (LRO WAC) image (100 m/pixel) overlaid with Lunar Prospector Th abundance data (2° × 2°/pixel; Prettyman et al., 2006). "A" and "L" represent the locations of Apollo and Luna sampling sites, and CE-5 represents the sampling site of Chang'e-5. The projection is Mercator centered at Mare Imbirum. (b) The prominent ray system around Lalande shown by LRO WAC image. The projection is Mercator centered at Lalande crater. Credit of WAC image: NASA/GSFC/Arizona State University; credit of Lunar Prospector Th abundance data: NASA/Washington University, St. Louis.

Furthermore, even though in the same Copernican period, the absolute ages of Lalande estimated from different studies also range a lot: Li et al. (2018) obtained AMAs of ~40–90 Ma by the cumulative size-frequency distributions (CSFDs) inside the rim and on the ejecta deposits near the rim of Lalande based on Lunar Reconnaissance Orbiter Narrow Angle Camera (LROC NAC) images (Robinson et al., 2010), while Mazrouei et al. (2019) estimated an age of 495 Ma for Lalande based on the rock abundance (RA) of crater ejecta obtained from LRO Diviner thermophysical measurements (Bandfield et al., 2011; Ghent et al., 2014). Is the formation age of Lalande consistent with the other radio-isotopic ages recorded in SaU 169 (e.g., ~200 Ma)?

In this work, we re-evaluate the crater statistics of Lalande ejecta blanket and estimate its formation age in a thorough way to verify whether this crater is possible to be one source region of SaU 169 meteorite, the most KREEP-rich sample. The possible influence of pre-existing craters of Lalande impact is also quantitatively analyzed to obtain a more reliable model age. Our clearance on the source region of SaU 169 meteorite can be used to interpret previous measurements concerning this rock and improve our understanding of lunar KREEP.

2. Data and method

2.1. CSFD measurements and image data

Continuous ejecta blankets and impact melt ponds are among the most obvious terrains formed during the impact cratering processes (Melosh, 1989) and are thus commonly used as crater population working areas to date the host crater. However, considerable age discrepancies are often observed among the two types of terrains: measurement on the impact melt ponds usually yielded younger ages than those from the continuous ejecta blankets (e.g., Hartmann, 1968; Strom and Fielder, 1968; van der Bogert et al., 2010; Hiesinger et al., 2012). These crater population differences from coeval surface terrains are commonly attributed to a range of factors including different target

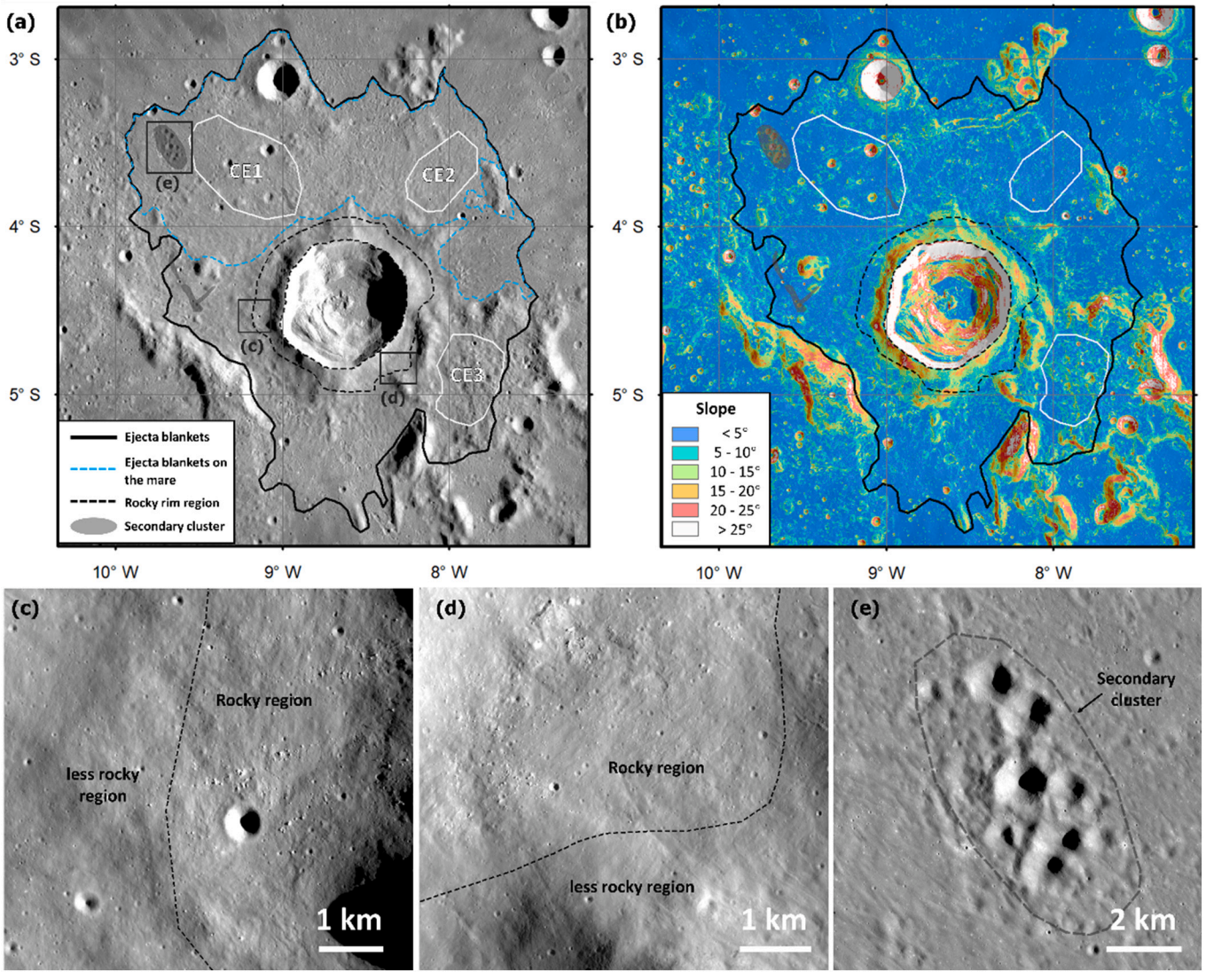


Fig. 2. Crater count working areas for dating the Lalande crater. (a) Regional geologic context, Kaguya Terrain Camera (TC) morning Map (10 m/ pixel; Haruyama et al., 2008). (b) Slope map derived from the SELENE/Kaguya TC + Lunar Reconnaissance Orbiter (LRO) Lunar Orbiter Laser Altimeter (LOLA) merged Digital Elevation Model (SLDEM2015; 512 pixel/degree; Barker et al., 2016) overlaying on the TC morning images of (a). The boundaries of Lalande's ejecta blankets (Fortezzo et al., 2020), ejecta blankets on mare (Nelson et al., 2014) and rocky rim region are delineated by solid black, dashed blue, and dashed black curves, respectively. The regions of secondary crater clusters are marked by filled grey polygons. (c)–(d) TC morning images showing the morphological characteristics of rocky regions in the vicinity of the rim crest. (e) An TC image of an obvious secondary crater cluster. All figures are projected in Mercator projection centered at Lalande and north is toward the top. Credit of Kaguya TC image: JAXA; credit of SLDEM2015 topography data: NASA/JAXA/GSFC/Washington University, St. Louis. (For interpretation of the references to colour in this figure legend, the reader is referred to the web version of this article.)

characteristics and self-secondary cratering (e.g., Shoemaker et al., 1968; Schultz et al., 1977; Dundas et al., 2010; Xie et al., 2019). As crater count measurement on the ejecta blankets of major impact basins/craters, for instance, Nectaris, Imbrium, and Copernicus, are traditionally used to establish and calibrate the lunar cratering chronology function (e.g., Neukum et al., 2001; Robbins, 2014), model ages derived from crater counts on ejecta blankets are usually more consistent with the radio-isotopic and exposure ages of Apollo samples than those from impact melt ponds, especially for the crater dating of young craters (e.g, Hiesinger et al., 2012). Therefore, we carefully select three regions termed CE1, CE2, and CE3 on the ejecta blankets (Fig. 2a,b) as crater population working areas to date the Lalande crater. The boundary of Lalande's continuous ejecta blankets (Fig. 2) is delineated according to the geologic map of Fortezzo et al. (2020). In order to verify the difference of the CSFDs between lunar mare and highlands, CE1 and CE2 are superposed on the extensive mare plains to the north and CE3 is superposed on the hummocky highland terrains in the south of Lalande crater, with the boundary of mare delineated by Nelson et al. (2014). Obvious secondary clusters (based on their morphological characteristics, Fig. 2a, b, e; Oberbeck and Morrison, 1974; Shoemaker, 1962), steep topography (with SLDEM slope larger than 10° for CE1 and CE2 and slope larger than 15° for CE3; Fig. 2b; Xiao and Strom, 2012), and rocky regions surrounding the Lalande rim (Fig. 2 a–d; Williams et al., 2014) are excluded from CE1-CE3 areas to minimize the influence of complicated topography and surface textures on the crater retention and identification, and hence improve statistic reliability of crater dating. The crater counts on the rocky rim region (an annulus region encircling Lalande's rim crest with steep slopes and abundant rocks, Fig. 2a-d) are also conducted for comparison.

Kaguya Terrain Camera (TC) images (10 m/pixel; Haruyama et al., 2008) with variable illumination conditions (morning, evening, and ortho) are used for crater identification and measurement. Given the Kaguya TC image resolution and the required 10 image pixels for complete and accurate crater counts (e.g., Wang et al., 2020), we only measure impact craters with diameters (D) larger than 100 m using the CraterTools software extension for ESRI's ArcGIS, which creates each crater circle using three manually picked points on the crater rim (Kneissl et al., 2011). For the working areas in this study, the resolution of Kaguya TC is sufficient to count an adequate number of craters.

By morphological investigations, we find that the ejecta of Lalande is not thick enough to completely bury all the craters formed before the Lalande crater (Fig. 3). For convenience, we term craters formed prior to the Lalande crater as "pre-Lalande craters", and accordingly, we term craters formed after the emplacement of Lalande's ejecta blankets as "post-Lalande craters". Based on the morphological criteria that craters with destructive rim crests and filled by ejecta radial to Lalande crater, we exclude those obvious pre-Lalande craters in CE1 to CE3 area with the assist of LROC NAC images (~1 m/pixel) (Fig. 3). We need to note that, in practice, the identification of pre-Lalande craters is sometimes difficult and less complete, but fortunately the influence of these craters can be separated in the CSFD plots (see further descriptions in section 3.2).

To investigate the effects of pre-Lalande craters on the age determination, we count all impact craters (D > 100 m) on Lalande's ejecta blankets on the mare (Fig. 2a) without the exclusion of pre-Lalande craters. Obvious secondary clusters are excluded in all the crater

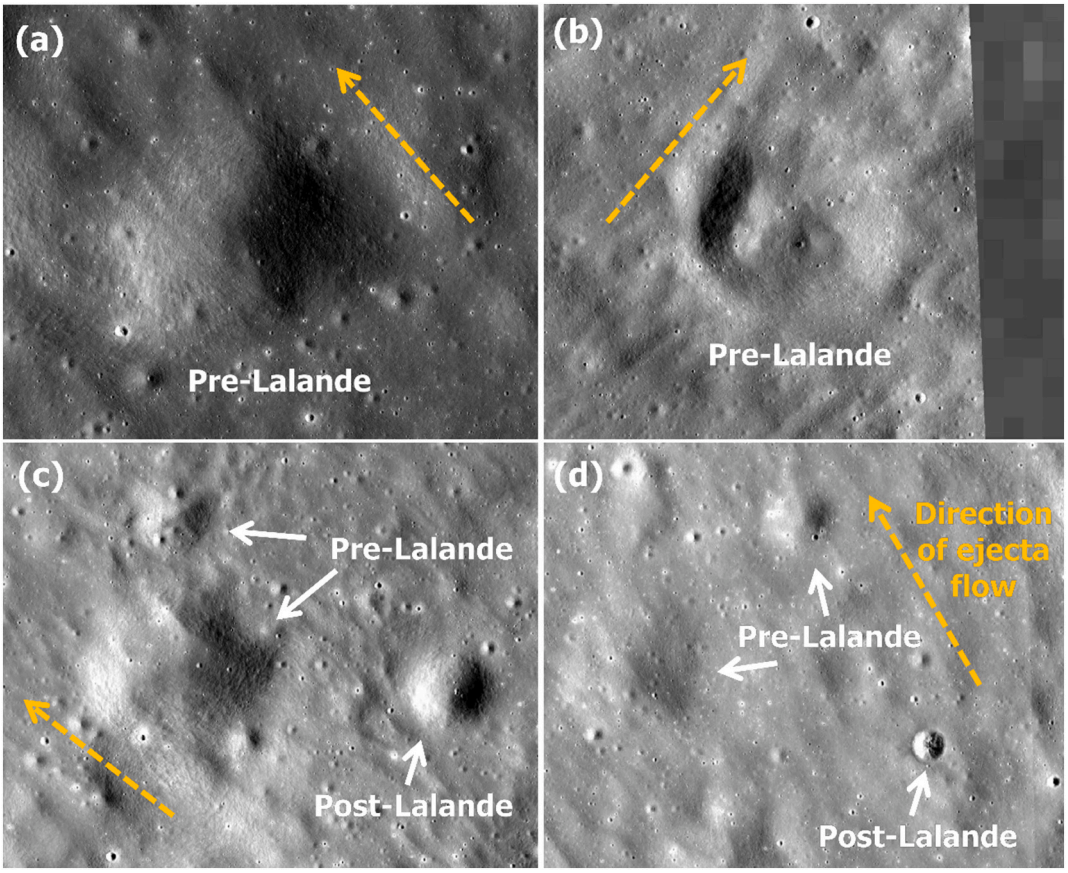


Fig. 3. LROC NAC images of examples of pre- and post-Lalande craters on the ejecta blankets of Lalande: (a) A pre-Lalande crater (3.74°S, 9.16°W) of ~1.1 km in diameter, (b) a pre-Lalande crater (3.97°S, 7.52°W) of ~1.0 km in diameter, (c) two pre-Lalande craters (3.69°S, 9.51°W and 3.73°S, 9.50°W) of ~560 m and ~ 1.3 km in diameter, and a post-Lalande crater (3.74°S, 9.44°W) of ~650 m in diameter, and (d) two pre-Lalande craters (3.39°S, 9.48°W and 3.36°S, 9.44°W) of ~1.0 km and ~ 440 m in diameter, and a post-Lalande crater (3.41°S, 9.41°W) of ~220 m in diameter. The orange dashed arrows show the directions of Lalande's ejecta flows. All figures are projected in an equidistant cylindrical projection and north is toward the top. Credit of NAC images: NASA/GSFC/Arizona State University.

counts and steep topography is only excluded in CE1-CE3 regions (Fig. 2a, b).

2.2. Age determination from CSFDs

The basic principle of crater population dating is that on a homogeneous geologic unit, the older surface has a higher cumulative primary crater density ρ (i.e., frequency) for a given crater size range before the crater equilibrium/saturation status is reached. We derive the CSFDs of the identified craters according to the standard procedures, which have been described in many classical literatures (e.g., Crater Analysis Techniques Working Group, 1979; Neukum, 1983; Hiesinger et al., 2000; Fassett, 2016).

By fitting the observed CSFDs to the crater production function (PF), we can derive the cumulative crater density for $D \geq 1$ km (i.e., $N(1)$ in km^{-2}). The fitting procedures are performed by the CraterStats software (Michael and Neukum, 2010; Michael, 2013), and the crater PF of Neukum et al. (2001) is adopted in this study:

$$log_{10}N(D) = a_0 + \sum_{n=1}^{11} a_n (log_{10}D)^n \ (10\ \text{m} < \text{D} < 300\ \text{km}) \quad (1)$$

where $N(D)$ (in km^{-2}) is the cumulative crater density with craters larger than D (in km).

Three chronology functions (CFs) of Neukum et al. (2001; Neukum CF hereafter), Robbins (2014; Robbins CF hereafter), and Yue et al. (2022; Yue CF hereafter) are employed to calculate the AMAs from $N(1)$ values obtained in this study:

$$\text{Neukum CF}: N(1) = 5.44{\cdot}10^{-14}\ (exp(6.93\ T) - 1\ ) + 8.38{\cdot}10^{-4}\ T \quad (2)$$

$$\text{Robbins CF}: N(1) = 7.26{\cdot}10^{-41}\ (exp(22.6\ T) - 1\ ) + 9.49{\cdot}10^{-4}\ T + 1.88{\cdot}10^{-4}\ T^2 \quad (3)$$

$$\text{Yue CF}: N(1) = 1.089{\cdot}10^{-13}\ (exp(6.757\ T) - 1\ ) + 7.660{\cdot}10^{-4}\ T \quad (4)$$

where T is the AMA in billion years (Ga).

The former two chronology functions are established from the similar anchor points of radio-isotopic ages of returned lunar samples, but different crater counts on Apollo and LROC image data for the sampling areas, respectively. The most recent CF of Yue et al. (2022) is updated by incorporating the radiometric age of Chang'e-5 samples.

Nevertheless, for the age ranges ($T < 0.5$ Ga and $T > 3.8$ Ga) discussed in this study, both AMAs derived from the Robbins CF and Yue CF have minor differences compared with that from Neukum CF (<70 Ma for $T < 0.5$ Ga and <90 Ma for $T > 3.8$ Ga, see Table 1 for details). Therefore, we prefer to use the ages derived from the Neukum CF for direct comparisons since previous age estimations are commonly based on the Neukum CF.

2.3. The distribution of Lalande's ejecta thickness and the smallest survival pre-Lalande craters

The primary ejecta materials surrounding the primary crater are generally the thickest at the crater's rim crest and decay exponentially with increasing range from crater center (e.g., McGetchin et al., 1973). If the ejecta are not sufficiently thick to completely bury all the pre-existing craters around the host crater, crater populations formed both before and after the host crater could co-exist on the primary crater ejecta blankets, which may potentially affect the crater counts and biased the age determination of the primary crater. Here, we quantitatively estimate the influence of pre-existing craters on the age determination of Lalande crater based on the empirical distribution model of ejecta thickness.

Assuming the ejecta distribution is symmetric and not affected by the pre-existing topography, the ejecta thickness distribution surrounding a primary crater can be estimated by the model of Pike (1974):

$$t(r) = 0.033R_t(r/R_t)^{-3.0} \quad (4)$$

where $t(r)$ is the primary ejecta thickness at one location outside the crater rim, r is the spherical distance from this location to the crater center, and R_t is the transient rim radius of the crater. The transient rim radius of Lalande can be computed by the expression $R_t = R_{SC}^{0.15}R^{0.85}$ for complex craters (Croft, 1985), where $R = 11.8$ km is the final rim radius of Lalande, and $R_{SC} = 9.5$ km is the transition radius from simple to complex craters on the Moon (Pike, 1980). In addition, since the range of Lalande's continuous ejecta blankets from the crater crest (up to ~40 km) is much smaller than the lunar radius (1737.4 km), the effect of the curvature of the Moon on ejecta deposition can be very negligible and neglected (Haskin et al., 2003; Xie et al., 2020; Xu et al., 2021).

According to the case studies of the Orientale and Schrödinger basins, the thickness of ejecta filling in a pre-existing crater is approximately 3 times of the ejecta deposited on a flat terrain due to the concave-upward shape of crater cavity (Xie and Zhu, 2016; Xu and Xie, 2020). Applying this relationship established from huge impact basins to smaller complex craters, the thicknesses of ejecta deposited inside pre-Lalande craters T_{inner} are estimated correspondingly. Furthermore, given the depth-to-diameter (d/D) ratios of small fresh lunar craters (class A) measured by Stopar et al. (2017) and without the consideration of crater degradations, the critical diameters $D_c(r)$ of the craters that are just completely buried by Lalande's primary ejecta (i.e.,

Table 1
Summary of the Cumulative Size-Frequency Distributions (CSFDs) and Absolute Model Ages (AMAs) of various areas on the Lalande crater ejecta.

Unit	Crater counting area (km^2)	Crater diameter for age fitting	Number of craters for age fitting	$N(1)$ (km^{-2})	AMA (Neukum CF)	AMA (Robbins CF)	AMA (Yue CF)
CE1	253	100–160 m	179	3.25 (± 0.20) × 10^{-4}	**390 ± 20 Ma**[*]	320 ± 20 Ma	420 ± 30 Ma
		≥ 350 m	21	1.86 (± 0.40) × 10^{-3}	2.2 ± 0.5 Ga	1.5 ± 0.3 Ga	2.4 ± 0.5 Ga
CE2	118	100–170 m	132	3.62 (± 0.29) × 10^{-4}	**430 ± 30 Ma**	360 ± 30 Ma	470 ± 40 Ma
CE3	152	100–170 m	140	3.64 (± 0.27) × 10^{-4}	**430 ± 30 Ma**	360 ± 20 Ma	470 ± 40 Ma
Sum of CE1 to CE3	523	100–170 m	462	3.43 (± 0.14) × 10^{-4}	**410 ± 20 Ma**	340 ± 10 Ma	450 ± 20 Ma
Rocky rim rgion	334	≥ 100 m	232	1.89 (± 0.12) × 10^{-4}	**230 ± 10 Ma**	190 ± 10 Ma	250 ± 20 Ma
Ejecta blankets on the mare	1780	100–170 m	1540	3.32 (± 0.07) × 10^{-4}	**400 ± 9 Ma**	330 ± 7 Ma	430 ± 10 Ma
		≥ 1.2 km	12	1.86 (± 0.53) × 10^{-2}	**$3.8^{+0.04}_{-0.06}$ Ga**	$3.9^{+0.02}_{-0.03}$ Ga	$3.8^{+0.04}_{-0.06}$ Ga

[*] The ages in bold fonts are results used to compare with previous studies.

the smallest survival pre-Lalande craters) can be estimated as:

$$D_c = \begin{cases} T_{inner}/0.125, & 40\ m < D < 100\ m \\ T_{inner}/0.152, & 100\ m < D < 200\ m \\ T_{inner}/0.166, & 200\ m < D < 400\ m \\ T_{inner}/0.209, & 400\ m < D < 10\ km \end{cases} \quad (5)$$

3. Results

3.1. Crater CSFD measurements of Lalande's ejecta blankets

For the crater counts in regions CE1 to CE3 (Supplementary Table S1-S3), the CSFD plots in the diameter range of ~100–170 m lies very close to certain isochrons, and have similar fitted $N(1)$ values of (3.25 ± 0.20) × 10^{-4} km^{-2}, (3.62 ± 0.29) × 10^{-4} km^{-2}, and (3.64 ± 0.27) × 10^{-4} km^{-2}, respectively. Under the Neukum CF, these $N(1)$ values would project AMAs of 390 ± 20 Ma, 430 ± 30 Ma, and 430 ± 30 Ma, respectively (Fig. 4a-c and Table 1). These ages are very close to each other within their uncertainties, suggesting that the different CSFDs of pre-Lalande craters on mare and highlands do not affect the observed CSFDs and age determination on Lalande's ejecta blankets. We derive an AMA of 410 ± 20 Ma (CSFD-fitted $N(1)$ value of (3.43 ± 0.14) × 10^{-4} km^{-2}) by combing all the crater counts in CECE1–CECE3 areas (Fig. 4d). For craters larger than ~170 m, the CSFDs for CECE1–CE3 show some degrees of deviations from the isochrons. The CSFDs for craters ≥350 m in CE1 can be fitted with an isochron and report a much older age of 2.2 ± 0.5 Ga ($N(1)$ = (1.86 ± 0.40) × 10^{-3} km^{-2}), indicating a possible re-surfacing event and the mixture of two crater populations on the continuous ejecta blankets of Lalande.

Two crater populations are also observed on the entire ejecta blankets on the mare (Fig. 4e, Supplementary Table S4): 1) Fitting of craters ~110–170 m in diameter derives an AMA of 400 ± 9 Ma ($N(1)$ = (3.32 ± 0.07) × 10^{-4} km^{-2}), very close to the age of combined CE1– CE3 regions. 2) Fitting of craters ≥1.2 km in diameter obtains a much older AMA of $3.8^{+0.04}_{-0.06}$ Ga ($N(1)$ = (1.86 ± 0.53) × 10^{-2} km^{-2}), indicating an older deposits emplaced before the Lalande impact event.

For crater counts on the rocky rim region (Fig. 4e), the CSFDs yield an considerably younger AMA of 230 ± 10 Ma ($N(1)$ = (1.89 ± 0.12) × 10^{-4} km^{-2}). This younger AMA is likely caused by the presence of large boulders that hinder the efficiency of crater formation (e.g, Williams et al., 2014) and steep topography that erases small craters efficiently due to the mass wasting process (e.g., Xiao and Strom, 2012). Therefore, the crater counts on this region tend to underestimate the formation time of Lalande crater.

3.2. The effect of ejecta burial and pre-Lalande craters

Based on the empirical distribution of ejecta thickness model described in section 2.3, we calculate that the ejecta thicknesses of Lalande crater are ~340 m at the rim crest and decrease to ~9 m at a distance of ~40 km, the farthest location for our crater count working areas CE1-CE3. Correspondingly, the thicknesses of ejecta deposited within pre-Lalande craters T_{inner} are estimated to be ~1 km–26 m (Fig. 5a). As a result, the diameters of smallest survival pre-Lalande craters $D_c(r)$ are ~5 km at Lalande's rim crest and decrease rapidly to ~170 m at a distance of ~40 km from crater center (Fig. 5b). As shown in Fig. 5b, at a certain distance from Lalande's center, all pre-existing craters smaller than the smallest survival diameter would be completely buried by Lalande's ejecta and cannot survive the Lalande impact event. Conversely, all observed craters smaller than this critical diameter should basically postdate the Lalande impact, while all pre-existing craters larger than this critical diameter can be only partially buried and thus can potentially survive and been observed. So, all observed craters on the Lalande ejecta blankets larger than these critical diameters contain a combination of almost all pre-existing and subsequent craters.

For the range of CE1-CE3 areas (~20–40 km from Lalande crater center), the corresponding smallest survival pre-Lalande craters are estimated to be ~1 km-170 m in diameter. All pre-Lalande craters smaller than ~170 m and a portion of pre-Lalande craters of ~170 m–1 km in diameter should have been completely buried by Lalande's ejecta materials (Fig. 5b). Based on these modelling estimations, we conclude that the effect of pre-Lalande craters on the dating results (410 ± 20 Ma) by fitting small craters <~170 m in diameter can be negligible (if any) and this age reflect the formation age of Lalande crater. The very close dating results from different working areas (CE1-CE3) further validate our small crater population measurements. In addition, because all craters D < ~170 m on CE1-CE3 are expected to accumulate from the same reset surface conditions (i.e., totally re-surfaced by Lalande's ejecta), there should have been negligible difference between mare (CE1 and CE2) and highlands (CE3) in the CSFDs of this diameter range, as we observed in Fig. 4a-c.

The pronounced deflections from isochrons observed at larger diameters (> ~ 170 m; Fig. 4a,e) can be attributed to the population of some survived pre-Lalande craters (~170 m–1 km), which may cause an overestimated age as we observed for craters ≥350 m in CE1 area. We suggest this older age (2.2 ± 0.5 Ga) is of very little geological significance and cannot be linked to any geological event because the crater population is incomplete (a part of the pre-Lalande craters should have been erased). This observation also shows that although we have successfully excluded almost all pre-Lalande craters in 2CE2 and CE3 areas through morphological examinations (Figs. 3 and 4b, c), a small portion of pre-Lalande craters still remain in the crater measurements in CE1 area. This practice demonstrates the very challenging task for identifying pre-existing small craters on aged surface, as various modification processes (impact gardening, topographic degradation, etc) can modified the very subtle morphological evidence of the burial trace of ejecta flows.

4. Discussion

4.1. The formation age of Lalande crater

On the basis of optical maturity parameter (OMAT) value profiles derived from large (D ≥ 20 km) lunar ray craters, Grier et al. (2001) classified Lalande crater as the "intermediate age group", which has inferred ages between Tycho (~109 Ma) and Copernicus (~810 Ma) crater. In this study, we determine that Lalande crater has a formation age of 410 ± 20 Ma based on our crater counts on CE1-CE3 (Fig. 4a-d) and quantitative model-based estimations (Fig. 5b) and confirm that it is of Copernican period. Our age is very close to the age of 495 Ma obtained by Mazrouei et al. (2019) from LRO Diviner rock abundance measurements, and both these two ages fall well within the age range of ~109 Ma - 810 Ma (Grier et al., 2001), indicating that all the three results are broadly consistent with each other.

Similar to CE1 (Fig. 4a), the CSFDs for larger crater diameters (D ≥ 1.2 km) on the entire ejecta blankets on the mare (Fig. 4e) also fit a much older age of $3.8^{+0.04}_{-0.06}$ Ga (Fig. 4e) comparing to Lalande's formation age. Based on our estimations (Fig. 5b), none of the pre-Lalande craters D ≥ ~1.2 km would have been completely buried by Lalande's ejecta within the distance range of CE1-CE3, and thus, almost all craters form before and after Lalande on these regions could remain to now, if we do not consider the influence other re-surfacing processes. Therefore, we consider that the AMA of $3.8^{+0.04}_{-0.06}$ Ga represents the cumulative distributions of the combined all pre- and post-Lalande craters and reflects the age of local basalt unit (noting that we do not exclude pre-Lalande craters in this region as we do in regions CE1 to CE3) on which the ejecta blankets of Lalande crater is superposed. This age is close to the older age of IN4 mare unit (2.9/3.5 Ga; Hiesinger et al., 2003) which locates in the northern region near Lalande.

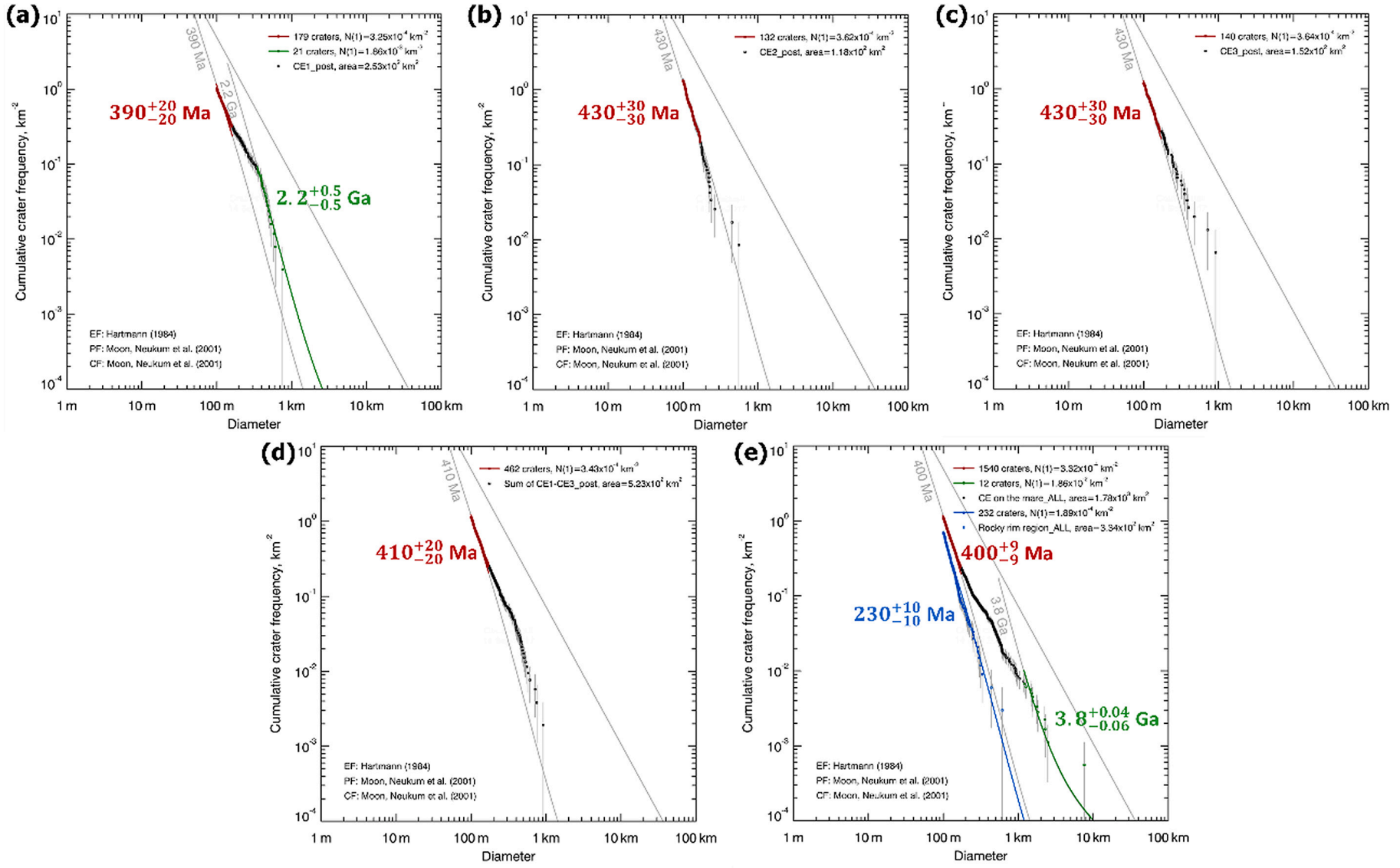


Fig. 4. CSFD plots and dating results for various studied regions on the ejecta blankets of Lalande crater (Fig. 2a): (a–c) regional crater observation of CE1, CE2, and CE3, respectively, with the exclusion of obvious pre-existing craters; (d) summed crater counting in CE1-CE3 areas, with the exclusion of obvious pre-existing craters; and (e) all craters on the rocky rim region and the entire ejecta blankets on the mare. The equilibrium function (EF) of Hartmann (1984) shows the crater saturation situations, and both the production function (PF) and the chronology functions (CF) are from Neukum et al. (2001). The uncertainties are defined by $\pm \rho/\sqrt{N}$, where ρ is the spatial density of crater and N is the total number of corresponding cumulative craters.

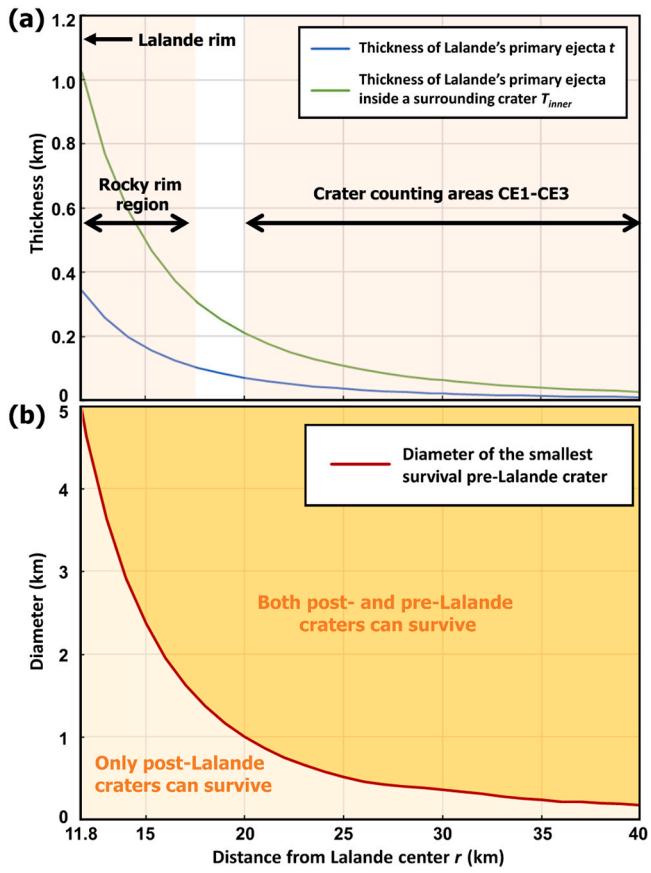


Fig. 5. The modelling estimations of the distributions of (a) Lalande's ejecta thickness and (b) the smallest survival pre-Lalande craters. The diameters of the smallest survival pre-Lalande craters are calculated from T_{inner} based on the ejecta distribution model of Pike (1974) and the depth-to-diameter (d/D) ratios measured by Stopar et al. (2017). We gradually reduce the ratios around the junction values (i.e., at diameters around 400 m, 200 m, and 100 m) for obtaining a smooth transition between each diameter interval.

4.2. Implication for the source region of the KREEP-rich lunar meteorite SaU 169

Integrating ages of many lunar craters estimated from Lunar Orbiter images obtained the 1960s (Baldwin, 1985) and elemental compositional mapping results (especially regolith Fe-Ti-Th concentrations), Gnos et al. (2004) suggested that the characteristics of the Lalande crater is most consistent with the age and compositional data of SaU 169. However, our updated crater population dating analysis using modern, uniform, high-resolution imagery and the latest understanding of lunar impact flux and radio-isotopic dating results cratering chronology model revealed that the age of Lalande is inconsistent with any of the radio-isotopic ages (~3.9 Ga, ~2.8 Ga, ~200 Ma, and <0.34 Ma; Gnos et al., 2004) recorded in SaU 169. Therefore, we conclude that Lalande crater is unlikely to be a source region of lunar meteorite SaU 169 because this impact event occurring at the timescale of 410 ± 20 Ma was not recorded in the meteoroid.

As for the much older age of 2.2–2.8 Ga obtained by Baldwin (1985), we consider the main reason is that his CSFDs measurements were mixed by the populations of pre-Lalande craters. The crater counts and dating of Baldwin (1985) are based on an assumption that the formation of an impact crater can totally erase the original surface and completely bury all the pre-existing craters in the locations of crater interior and ejecta blanket. However, our morphological investigations (Fig. 2), crater counts (Fig. 4 and section 3.1), and theoretical estimations (Fig. 5 and section 3.2) show that this assumption cannot be applied to the situation of Lalande, and the mixing of pre-Lalande craters will inevitably lead to an overestimated model age (Fig. 4a and section 4.1), especially considering that his crater counts are mainly conducted for relatively larger craters (D > 0.5 km) due to the limitation of image quality, the influence of larger craters (D > ~1 km) pre-Lalande craters may be more dominant (Fig. 5b). In addition, the possible influence of secondary craters cannot be ruled out, and Baldwin (1985) also noted that "the presence of substantial numbers of secondary craters" is suggested in the CSFDs measurements of Lalande. Besides, the widely accepted PFs and CFs such as Neukum et al. (2001) have not been well established at that time, which may also affect the accuracy of crater dating.

In addition, the similarities in chemistry, mineralogy, texture, and isotopic age between the high-Th IMBs of SaU 169 and Apollo 12 samples support that these high-Th IMBs may form in the same primary impact event (most likely to be the Imbrium event), experience one or more subsequent impacts and remobilizations, and then be delivered from the same area of the Procellarum KREEP Terrane to their launch/current locations (Zeigler et al., 2006; Liu et al., 2012). However, samples collected by the Apollo 14 mission from a location between Lalande crater and Apollo 12 site do not contain such high-Th IMBs (e.g., Jolliff et al., 1991; Korotev et al., 2011). These observations also disapprove Lalande as a source region of the Apollo 12 and SaU 169 IMBs, otherwise, similar IMBs should have also been delivered to the Apollo 14 site. In combination with our age determination results, the impact event of Lalande is unlikely to play a role in the excavation and remobilization processes of SaU 169, and the unique high-Th meteorite SaU 169 is yet to search other more likely source region linking to its recorded impact events at ~2800 Ma and ~ 200 Ma. Since this study has excluded Lalande crater as the potential source of SaU 169, a revisit to the other Th hotspots such as regions around Aristarchus crater, Aristillus crater, and Montes Carpathus-Fra Mauro (Gnos et al., 2004) are a promising effort.

5. Conclusion

In this study, we conduct crater counts on several regions of Lalande's ejecta blankets and quantitatively assess the influence of pre-existing craters on the age determination of Lalande crater. Based on these analyses, we obtain that Lalande crater is a Copernican crater with a formation age of 410 ± 20 Ma. The formation age of Lalande is inconsistent with any impact events recorded in meteorite SaU 169, so Lalande crater is unlikely to be the source region of this meteorite.

We find that the crater statistics of Lalande are heavily influenced by the existence of pre-Lalande craters larger than ~170 m in diameter. Incorporating these pre-existing craters would lead to a largely overestimated age of Lalande crater and may be the main reason of the much larger age of ~2.5 Ga obtained by the crater dating of Baldwin (1985). According to our quantitative estimation, it is expected that all pre-Lalande craters larger than ~1 km on the counting regions in this study could survive Lalande's ejecta burial and remain observed. The population of these larger craters contains surface age information of the underlying mare deposits with an Imbrian age of $3.8^{+0.04}_{-0.06}$ Ga.

Our case study of Lalande crater sheds light on the source region of lunar meteorite SaU 169 and indicates that the age determination using small crater populations should be treated with very caution, and fully understanding the geologic context of the surface is extremely essential for a more reliable dating result.

Declaration of Competing Interest

None.

Acknowledgments

This work was supported by the Science and Technology Development Fund, Macau SAR (File no. SKL-LPS(MUST)-2021-2023), the

opening fund of State Key Laboratory of Lunar and Planetary Sciences (Macau University of Science and Technology), the pre-research project on Civil Aerospace Technologies No. D020204 funded by China National Space Administration (CNSA), Young Scholars Program of Shandong University, Weihai (No. 202207), and the National Natural Science Foundation of China (42003053). All original LRO data can be found in the NASA Planetary Data System Geosciences Node (https://pds-geosciences.wustl.edu/), Kaguya/SELENE TC image data can be downloaded from SELENE Data Archive (https://darts.isas.jaxa.jp/planet/pdap/selene/), and SLDEM2015 topography data are available at the Planetary Geodynamics Data Archive (PGDA) (https://pgda.gsfc.nasa.gov/products/54).

Appendix A. Supplementary data

Supplementary data to this article can be found online at https://doi.org/10.1016/j.icarus.2022.115166.

References

Al-Kathiri, A., Gnos, E., Hofmann, B.A., 2007. The regolith portion of the lunar meteorite Sayh al Uhaymir 169. Meteorit. Planet. Sci. 42 (12), 2137–2152.
Baldwin, R.B., 1985. Relative and absolute ages of individual craters and the rate of infalls on the moon in the post-Imbrium period. Icarus 61 (1), 63–91.
Bandfield, J.L., Ghent, R.R., Vasavada, A.R., Paige, D.A., Lawrence, S.J., Robinson, M.S., 2011. Lunar surface rock abundance and regolith fines temperatures derived from LRO diviner radiometer data. J. Geophys. Res. Planets 116 (E12).
Barker, M.K., Mazarico, E., Neumann, G.A., Zuber, M.T., Haruyama, J., Smith, D.E., 2016. A new lunar digital elevation model from the lunar orbiter laser altimeter and SELENE terrain camera. Icarus 273, 346–355.
Crater Analysis Techniques Working Group, 1979. Standard techniques for presentation and analysis of crater size-frequency data. Icarus 37 (2), 467–474. https://doi.org/10.1016/0019-1035(79)90009-5.
Croft, S.K., 1985. The scaling of complex craters. J. Geophys. Res. 90 (S02), C828–C842. https://doi.org/10.1029/JB090iS02p0C828.
Dundas, C.M., Keszthelyi, L.P., Bray, V.J., McEwen, A.S., 2010. Role of material properties in the cratering record of young platy-ridged lava on Mars. Geophys. Res. Lett. 37 (12).
Elphic, R.C., Lawrence, D.J., Feldman, W.C., Barraclough, B.L., Maurice, S., Binder, A.B., Lucey, P.G., 1998. Lunar Fe and Ti abundances: comparison of lunar prospector and Clementine data. Science 281 (5382), 1493–1496.
Fassett, C.I., 2016. Analysis of impact crater populations and the geochronology of planetary surfaces in the inner solar system. J. Geophys. Res. Planets 121 (10), 1900–1926. https://doi.org/10.1002/2016JE005094.
Fortezzo, C.M., Spudis, P.D., Harrel, S.L., 2020. Release of the digital unified global geologic map of the moon at 1: 5,000,000-scale. LPI 2326, 2760.
Ghent, R.R., Hayne, P.O., Bandfield, J.L., Campbell, B.A., Allen, C.C., Carter, L.M., Paige, D.A., 2014. Constraints on the recent rate of lunar ejecta breakdown and implications for crater ages. Geology 42 (12), 1059–1062.
Gnos, E., Hofmann, B.A., Al-Kathiri, A., Lorenzetti, S., Eugster, O., Whitehouse, M.J., Greenwood, R.C., 2004. Pinpointing the source of a lunar meteorite: implications for the evolution of the moon. Science 305 (5684), 657–659.
Grier, J.A., McEwen, A.S., Lucey, P.G., Milazzo, M., Strom, R.G., 2001. Optical maturity of ejecta from large rayed lunar craters. J. Geophys. Res. Planets 106 (E12), 32847–32862.
Hartmann, W.K., 1968. Lunar crater counts. VI: the young craters Tycho, Aristarchus, and Copernicus. Lunar Planet. Lab. Comm. 8, 145–156.
Hartmann, W.K., 1984. Does crater “saturation equilibrium” occur in the solar system? Icarus 60 (1), 56–74.
Haruyama, J., Matsunaga, T., Ohtake, M., Morota, T., Honda, C., Yokota, Y., Ogawa, Y., 2008. Global lunar-surface mapping experiment using the lunar imager/spectrometer on SELENE. Earth, Planets Space 60 (4), 243–255.
Haskin, L.A., Moss, B.E., McKinnon, W.B., 2003. On estimating contributions of basin ejecta to regolith deposits at lunar sites. Meteorit. Planet. Sci. 38 (1), 13–33.
Hawke, B.R., Blewett, D.T., Lucey, P.G., Smith, G.A., Bell III, J.F., Campbell, B.A., Robinson, M.S., 2004. The origin of lunar crater rays. Icarus 170 (1), 1–16.
Heiken, G.H., Vaniman, D.T., French, B.M., 1991. Lunar Sourcebook, a user’s Guide to the Moon.
Hiesinger, H., Jaumann, R., Neukum, G., Head III, J.W., 2000. Ages of mare basalts on the lunar nearside. J. Geophys. Res. Planets 105 (E12), 29239–29275. https://doi.org/10.1029/2000JE001244.
Hiesinger, H., Head III, J.W., Wolf, U., Jaumann, R., Neukum, G., 2003. Ages and stratigraphy of mare basalts in oceanus procellarum, mare nubium, mare cognitum, and mare insularum. J. Geophys. Res. Planets 108 (E7).
Hiesinger, H.V., van Der Bogert, C.H., Pasckert, J.H., Funcke, L., Giacomini, L., Ostrach, L.R., Robinson, M.S., 2012. How old are young lunar craters? J. Geophys. Res. Planets 117 (E12).
Jolliff, B.L., Korotev, R.L., Haskin, L.A., 1991. Geochemistry of 2–4-mm particles from Apollo 14 soil (14161) and implications regarding igneous components and soil-forming processes. In: Lunar and Planetary Science Conference Proceedings, Vol. 21, pp. 193–219.
Jolliff, B.L., Gillis, J.J., Haskin, L.A., Korotev, R.L., Wieczorek, M.A., 2000. Major lunar crustal terranes: surface expressions and crust-mantle origins. J. Geophys. Res. Planets 105 (E2), 4197–4216.
Kneissl, T., van Gasselt, S., Neukum, G., 2011. Map-projection-independent crater size-frequency determination in GIS environments—new software tool for ArcGIS. Planet. Space Sci. 59 (11–12), 1243–1254. https://doi.org/10.1016/j.pss.2010.03.015.
Korotev, R.L., 2004. A unique chunk of the moon. Science 305 (5684), 622–623.
Korotev, R.L., 2005. Lunar geochemistry as told by lunar meteorites. Geochemistry 65 (4), 297–346.
Korotev, R.L., Zeigler, R.A., Jolliff, B.L., Irvin, A.J., Bunch, T.E., 2009. Compositional and lithological diversity among brecciated lunar meteorites of intermediate iron concentration. Meteorit. Planet. Sci. 44 (9), 1287–1322.
Korotev, R.L., Jolliff, B.L., Zeigler, R.A., Seddio, S.M., Haskin, L.A., 2011. Apollo 12 revisited. Geochim. Cosmochim. Acta 75 (6), 1540–1573.
Lawrence, D.J., Feldman, W.C., Barraclough, B.L., Binder, A.B., Elphic, R.C., Maurice, S., Prettyman, T.H., 1999. High resolution measurements of absolute thorium abundances on the lunar surface. Geophys. Res. Lett. 26 (17), 2681–2684.
Lawrence, D.J., Elphic, R.C., Feldman, W.C., Prettyman, T.H., Gasnault, O., Maurice, S., 2003. Small-area thorium features on the lunar surface. J. Geophys. Res. Planets 108 (E9).
Li, B., Ling, Z., Zhang, J., Chen, J., Liu, C., Bi, X., 2018. Geological mapping of lunar highland crater Lalande: topographic configuration, morphology and cratering process. Planet. Space Sci. 151, 85–96.
Li, C., Hu, H., Yang, M.F., Pei, Z.Y., Zhou, Q., Ren, X., Ouyang, Z., 2022. Characteristics of the lunar samples returned by the Chang’E-5 mission. Natl. Sci. Rev., nwab188 https://doi.org/10.1093/nsr/nwab188.
Lin, Y., Shen, W., Liu, Y., Xu, L., Hofmann, B.A., Mao, Q., Li, X.H., 2012. Very high-K KREEP-rich clasts in the impact melt breccia of the lunar meteorite SaU 169: new constraints on the last residue of the lunar Magma Ocean. Geochim. Cosmochim. Acta 85, 19–40.
Liu, D., Jolliff, B.L., Zeigler, R.A., Korotev, R.L., Wan, Y., Xie, H., Wang, W., 2012. Comparative zircon U–Pb geochronology of impact melt breccias from Apollo 12 and lunar meteorite SaU 169, and implications for the age of the Imbrium impact. Earth Planet. Sci. Lett. 319, 277–286.
Mazrouei, S., Ghent, R.R., Bottke, W.F., Parker, A.H., Gernon, T.M., 2019. Earth and moon impact flux increased at the end of the Paleozoic. Science 363 (6424), 253–257.
McGetchin, T.R., Settle, M., Head, J.W., 1973. Radial thickness variation in impact crater ejecta: implications for lunar basin deposits. Earth Planet. Sci. Lett. 20 (2), 226–236.
Melosh, H.J., 1989. Impact Cratering: A Geologic Process. New York: Oxford University Press; Oxford: Clarendon Press.
Meyer Jr., C., 1977. Petrology, mineralogy and chemistry of KREEP basalt. Phys. Chem. Earth 10 (4, 19).
Michael, G.G., 2013. Planetary surface dating from crater size–frequency distribution measurements: multiple resurfacing episodes and differential isochron fitting. Icarus 226 (1), 885–890. https://doi.org/10.1016/j.icarus.2013.07.004.
Michael, G.G., Neukum, G., 2010. Planetary surface dating from crater size–frequency distribution measurements: partial resurfacing events and statistical age uncertainty. Earth Planet. Sci. Lett. 294 (3–4), 223–229. https://doi.org/10.1016/j.epsl.2009.12.041.
Nelson, D.M., Koeber, S.D., Daud, K., Robinson, M.S., Watters, T.R., Banks, M.E., Williams, N.R., 2014. Mapping lunar maria extents and lobate scarps using LROC image products. In: Lunar and Planetary Science Conference, p. 2861. No. 1777.
Neukum, G., 1983. Meteoritenbombardement und Datierung planetarer Oberflächen, Habilitation dissertation for faculty membership. Ludwig-Maximilians-University, Munich, 186.
Neukum, G., Ivanov, B.A., Hartmann, W.K., 2001. Cratering records in the inner solar system in relation to the lunar reference system. Chronol. Evol. Mars 55–86.
Oberbeck, V., Morrison, R., 1974. Laboratory simulation of the herringbone pattern associated with lunar secondary crater chains. The Moon 9 (3–4), 415–455. https://doi.org/10.1007/BF00562581.
Pike, R.J., 1974. Ejecta from large craters on the moon: comments on the geometric model of McGetchin et al. Earth Planet. Sci. Lett. 23 (3), 265–271. https://doi.org/10.1016/0012-821X(74)90114-9.
Pike, R.J., 1980. Control of crater morphology by gravity and target type-Mars, Earth, Moon. Proc. Lunar Planet. Sci. Conf. 11, 2159–2189.
Prettyman, T.H., Hagerty, J.J., Elphic, R.C., Feldman, W.C., Lawrence, D.J., McKinney, G.W., Vaniman, D.T., 2006. Elemental composition of the lunar surface: analysis of gamma ray spectroscopy data from Lunar Prospector. J. Geophys. Res. Planets 111 (E12).
Robbins, S.J., 2014. New crater calibrations for the lunar crater-age chronology. Earth Planet. Sci. Lett. 403, 188–198.
Robinson, M.S., Brylow, S.M., Tschimmel, M., Humm, D., Lawrence, S.J., Thomas, P.C., Hiesinger, H., 2010. Lunar reconnaissance orbiter camera (LROC) instrument overview. Space Sci. Rev. 150 (1), 81–124.
Russell, S.S., Zipfel, J., Folco, L., Jones, R., Grady, M.M., McCOY, T., Grossman, J.N., 2003. The Meteoritical bulletin, no. 87, 2003 July. Meteorit. Planet. Sci. 38 (S7), A189–A248.
Schultz, P.H., Greeley, R., Gault, D., 1977. Interprcting statistics of small lunar craters. In: Proc. Lunar Sci. Conf, 8th, pp. 3539–3564.
Shearer, C.K., Hess, P.C., Wieczorek, M.A., Pritchard, M.E., Parmentier, E.M., Borg, L.E., Wiechert, U., 2006. Thermal and magmatic evolution of the Moon. Rev. Mineral. Geochem. 60 (1), 365–518.

Shoemaker, E.M., 1962. Interpretation of lunar craters. In: Kopal, Z. (Ed.), Physics and Astronomy of the Moon. Academic Press, New York, pp. 283–360.
Shoemaker, E.M., Batson, R.M., Holt, H.E., Morris, E.C., Rennilson, J.J., Whitaker, E.A., 1968. Television observations from surveyor VII. In: Surveyor 7Mission Report. Part 2 - Science Results, Tech. Rep. 32–1264. Jet. Propul. Lab, Pasadena, Calif, pp. 9–76.
Smith, J.V., Anderson, A.T., Newton, R.C., Olsen, E.J., Wyllie, P.J., 1970. A petrologic model for the Moon based on petrogenesis, experimental petrology, and physical properties. J. Geol. 78 (4), 381–405.
Stöffler, D., Ryder, G., 2001. Stratigraphy and isotope ages of lunar geologic units: Chronological standard for the inner solar system. In: Chronology and evolution of Mars. Springer, Dordrecht, pp. 9–54.
Stopar, J.D., Robinson, M.S., Barnouin, O.S., McEwen, A.S., Speyerer, E.J., Henriksen, M. R., Sutton, S.S., 2017. Relative depths of simple craters and the nature of the lunar regolith. Icarus 298, 34–48.
Strom, R.G., Fielder, G., 1968. Multiphase development of the lunar crater Tycho. Nature 217, 611–615 doi:l0.1038/217611a0.
Tartèse, R., Anand, M., Joy, K.H., Franchi, I.A., 2014. H and Cl isotope systematics of apatite in brecciated lunar meteorites Northwest Africa 4472, Northwest Africa 773, Sayh al Uhaymir 169, and Kalahari 009. Meteorit. Planet. Sci. 49 (12), 2266–2289.
Tian, H.C., Wang, H., Chen, Y., Yang, W., Zhou, Q., Zhang, C., Wu, F.Y., 2021. Non-KREEP origin for Chang'e-5 basalts in the Procellarum KREEP terrane. Nature 600 (7887), 59–63.
van der Bogert, C.H., Hiesinger, H., McEwen, A.S., Dundas, C., Bray, V., Robinson, M.S., Team, L, 2010. Discrepancies between crater size-frequency distributions on ejecta and impact melt pools at lunar craters: An effect of differing target properties?. In: 41st Lunar and Planetary Science Conference, p. 2165. No. 1533.
Wang, Y., Xie, M., Xiao, Z., Cui, J., 2020. The minimum confidence limit for diameters in crater counts. Icarus 341, 113645.
Warren, P.H., 1985. The magma ocean concept and lunar evolution. Annu. Rev. Earth Planet. Sci. 13 (1), 201–240.
Warren, P.H., Wasson, J.T., 1979. The origin of KREEP. Rev. Geophys. 17 (1), 73–88.
Wilhelms, D.E., John, F., Trask, N.J., 1987. The Geologic History of the Moon. USGS Professional Paper 1348.
Williams, J.P., Paige, D.A., Plescia, J.B., Pathare, A.V., Robinson, M.S., 2014. Crater size-frequency distributions on the ejecta of Giordano Bruno. In: Lunar and Planetary Science Conference, p. 2882. No. 1777.
Wood, J.A., Dickey Jr., J.S., Marvin, U.B., Powell, B.N., 1970. Lunar anorthosites and a geophysical model of the moon. Geochim. Cosmochim. Acta Supplement 1, 965.
Xiao, Z., Strom, R.G., 2012. Problems determining relative and absolute ages using the small crater population. Icarus 220 (1), 254–267.
Xie, M., Zhu, M.H., 2016. Estimates of primary ejecta and local material for the Orientale basin: implications for the formation and ballistic sedimentation of multi-ring basins. Earth Planet. Sci. Lett. 440, 71–80.
Xie, M., Xiao, Z., Xu, A., 2019. Time-dependent production functions of lunar simple craters on layered targets with consideration of topographic degradation. Geophys. Res. Lett. 46 (20), 10987–10996.
Xie, M., Xiao, Z., Zhang, X., Xu, A., 2020. The provenance of regolith at the Chang'e-5 candidate landing region. J. Geophys. Res. Planets 125 (5), e2019JE006112.
Xing, W., Lin, Y., Zhang, C., Zhang, M., Hu, S., Hofmann, B.A., Gu, L., 2020. Discovery of reidite in the lunar meteorite Sayh al Uhaymir 169. Geophys. Res. Lett. 47 (21), e2020GL089583.
Xu, L., Xie, M., 2020. Ejecta thickness distribution of the Schrödinger Basin on the Moon. J. Geophys. Res. Planets 125 (12), e2020JE006506.
Xu, L., Zhang, X., Qiao, L., Lai, J., 2021. Evaluating the thickness and stratigraphy of ejecta materials at the Chang'e-4 landing site. Astron. J. 162 (1), 29.
Yue, Z., Di, K., Wan, W., Liu, Z., Gou, S., Liu, B., Ouyang, Z., 2022. Updated lunar cratering chronology model with the radiometric age of Chang'e-5 samples. Nat. Astronomy 1–5.
Zeigler, R.A., Korotev, R.L., Jolliff, B.L., 2006. Geochemistry and petrography of high-Th, mafic impact-melt breccia from Apollo 12 and Sayh Al Uhaymir 169. In: Lunar and Planetary Science Conference, p. 2366.
Zhang, B., Lin, Y., Moser, D.E., Hao, J., Shieh, S.R., Bouvier, A., 2019. Imbrium age for zircons in Apollo 17 south massif impact melt breccia 73155. J. Geophys. Res. Planets 124 (12), 3205–3218.